The Astrophysical Journal Letters, 890:L10 (7pp), 2020 February 10 https://doi.org/10.3847/2041-8213/ab70b7

Systematic Variations of CO $J = 2-1/1-0$ Ratio and Their Implications in The Nearby Barred Spiral Galaxy M83

Jin Koda[1,2], Tsuyoshi Sawada[3,4], Kazushi Sakamoto[5], Akihiko Hirota[3,4], Fumi Egusa[6], Samuel Boissier[7], Daniela Calzetti[8], Jennifer Donovan Meyer[9], Bruce G. Elmegreen[10], Armando Gil de Paz[11,12], Nanase Harada[5], Luis C. Ho[13,14], Masato I. N. Kobayashi[15], Nario Kuno[16,17], Sergio Martín[4,18], Kazuyuki Muraoka[19], Kouichiro Nakanishi[20,21], Nick Scoville[22], Mark Seibert[23], Catherine Vlahakis[9], and Yoshimasa Watanabe[24]
[1] Department of Physics and Astronomy, Stony Brook University, Stony Brook, NY 11794-3800, USA; jin.koda@stonybrook.edu
[2] Amanogawa Galaxy Astronomy Research Center, Kagoshima University, 890-0065, Kagoshima, Japan[25]
[3] NAOJ Chile, National Astronomical Observatory of Japan, Alonso de Córdova 3788, Office 61B, Vitacura, Santiago 763 0492, Chile
[4] Joint ALMA Observatory, Alonso de Córdova 3107, Vitacura, Santiago 763 0355, Chile
[5] Academia Sinica, Institute of Astronomy and Astrophysics, Taipei 10617, Taiwan
[6] Institute of Astronomy, Graduate School of Science, The University of Tokyo, 2-21-1 Osawa, Mitaka, Tokyo 181-0015, Japan
[7] Aix Marseille Univ., CNRS, CNES, Laboratoire d'Astrophysique de Marseille, Marseille, France
[8] Department of Astronomy, University of Massachusetts, Amherst, MA 01002, USA
[9] National Radio Astronomy Observatory, 520 Edgemont Road, Charlottesville, VA 22903-2475, USA
[10] IBM Research Division, T.J. Watson Research Center, 1101 Kitchawan Road, Yorktown Heights, NY 10598, USA
[11] Departamento de Física de la Tierra y Astrofísica, Universidad Complutense de Madrid, Plaza Ciencias 1, Madrid E-28040, Spain
[12] Instituto de Física de Partículas y del Cosmos (IPARCOS), Spain
[13] The Kavli Institute for Astronomy and Astrophysics, Peking University, 5 Yiheyuan Road, Haidian District, Beijing, 100871, People's Republic of China
[14] Department of Astronomy, Peking University, 5 Yiheyuan Road, Haidian District, Beijing, 100871, People's Republic of China
[15] Department of Earth and Space Science, Graduate School of Science, Osaka University, Osaka 560-0043, Japan
[16] Department of Physics, Graduate School of Pure and Applied Sciences, University of Tsukuba, 1-1-1 Ten-nodai, Tsukuba, Ibaraki 305-8577, Japan
[17] Tomonaga Center for the History of the Universe, University of Tsukuba, 1-1-1, Ten-nodai, Tsukuba, Ibaraki 305-8571, Japan
[18] European Southern Observatory, Alonso de Córdova, 3107, Vitacura, Santiago 763-0355, Chile
[19] Department of Physical Science, Graduate School of Science, Osaka Prefecture University, 1-1 Gakuen-cho, Naka-ku, Sakai, Osaka 599-8531, Japan
[20] National Astronomical Observatory of Japan, Mitaka, Tokyo 181-8588, Japan
[21] The Graduate University for Advanced Studies, SOKENDAI, Mitaka, Tokyo 181-8588, Japan
[22] California Institute of Technology, MC 249-17, 1200 East California Boulevard, Pasadena, CA 91125, USA
[23] Observatories of the Carnegie Institution for Science, Pasadena, CA 91101, USA
[24] College of Engineering, Nihon University, 1 Nakagawara, Tokusada, Tamuramachi, Koriyama, Fukushima 963-8642, Japan
Received 2019 December 10; revised 2020 January 5; accepted 2020 January 28; published 2020 February 11

Abstract

We present spatial variations of the CO $J = 2-1/1-0$ line ratio ($R_{21/10}$) in the barred spiral galaxy M83 using Total Power Array (single-dish telescopes) data from the Atacama Large Millimeter/submillimeter Array. While the intensities of these two lines correlate tightly, $R_{21/10}$ varies over the disk, with a disk average ratio of 0.69, and shows the galactic center and a two-arm spiral pattern. It is high ($\gtrsim$0.7) in regions of high molecular gas surface density ($\Sigma_{\rm mol}$), but ranges from low to high ratios in regions of low $\Sigma_{\rm mol}$. The ratio correlates well with the spatial distributions and intensities of far-ultraviolet (FUV) and infrared (IR) emissions, with FUV being the best correlated. It also correlates better with the ratio of specific intensities at 70 and 350 μm, a proxy for dust temperature, than with the IR intensities. Taken together, these results suggest either a direct or indirect link between the dust heating by the interstellar radiation field and the condition of giant molecular clouds (GMCs), even though no efficient mechanism is known for a thermal coupling of dust and bulk gas in GMCs. We speculate that the large spread of $R_{21/10}$ in low $\Sigma_{\rm mol}$ regions, mostly at the downstream sides of spiral arms, may be due to the evolution of massive stars after spiral arm passage. Having in a late phase escaped from the spiral arms and their parental clouds, they may contribute to the dust heating by FUV and gas heating by cosmic rays produced by supernovae.

Unified Astronomy Thesaurus concepts: Molecular gas (1073); Spiral galaxies (1560); Interstellar medium (847)

1. Introduction

The $J = 1$–0 line transition of carbon monoxide, CO(1–0), has been the yardstick for observations and calibrations of the molecular gas in the Milky Way (MW) and nearby galaxies (see Dame et al. 1987; Scoville & Sanders 1987; Fukui & Kawamura 2010; Heyer & Dame 2015, for review). Recently, this fundamental transition is being replaced by the higher excitation transition CO(2–1) on the assumption of a constant CO 2–1/1–0 line ratio ($R_{21/10}$; e.g., Leroy et al. 2009; Saintonge et al. 2018; Sun et al. 2018). Observations in CO(2–1) require much less time than those in CO(1–0) to achieve the same mass sensitivity especially at the Atacama Large Millimeter/submillimeter Array (ALMA) site (Sakamoto 2008; Watson & Koda 2017). Many nearby galaxy projects with ALMA employ CO(2–1) as an alternative to CO(1–0) to trace the bulk molecular gas.

The notion of a constant $R_{21/10}$ arose from analyses of past single-dish data on nearby galaxies (e.g., Bigiel et al. 2008; Sandstrom et al. 2013), with caveats (Leroy et al. 2009). The faint CO emission in the interarm regions was often undetected, and most of those analyses were limited to radial profiles after azimuthal averaging (hence washing out arm-interarm variations). Measurements of $R_{21/10}$ often suffered from calibration difficulties (Koda et al. 2012). For example, no obvious variation was found in M51 with earlier data (Garcia-Burillo et al. 1993), but

[25] visiting.

systematic variations between the spiral arms and interarm regions were found later, primarily due to improved observational instruments and techniques (Koda et al. 2012; Vlahakis et al. 2013).

It is known that $R_{21/10}$ is an important diagnostic tracer of the physical conditions of molecular gas. In the MW, $R_{21/10}$ changes systematically from 1.0–1.2 to 0.3–0.4 between spiral arms and interarm regions, from the galaxy center to the outer disk, and between star-forming and dormant giant molecular clouds (GMCs; Sakamoto et al. 1994, 1997; Oka et al. 1996; Hasegawa 1997; Falgarone et al. 1998; Seta et al. 1998; Sawada et al. 2001; Yoda et al. 2010; Nishimura et al. 2015). These variations in the MW and M51 can be interpreted as changes of a factor of 2–3 in temperature and/or density, according to the non-local thermodynamic equilibrium (non-LTE) calculations (Goldreich & Kwan 1974; Scoville & Solomon 1974; Koda et al. 2012). Besides these two galaxies, analyses of $R_{21/10}$ with well-calibrated data still remain rare even with single-dish telescopes. It is urgent to build up such accurate analyses given the growing amount of CO(2–1) observations of nearby galaxies.

Here we present another case, the barred spiral galaxy M83 at a distance of 4.5 Mpc (Thim et al. 2003), using new single-dish data from ALMA. In this galaxy, Crosthwaite et al. (2002) found an elevated $R_{21/10}$ in the interarm regions, contrary to the results in the MW and M51. The ratio appeared so high (>1) that it potentially indicated that optically thin CO emission dominates in the interarm regions and overshadows the emission from GMCs. Lundgren et al. (2004) also found a similar qualitative trend: an elevated, but lower (<1), $R_{21/10}$ in the interarm regions. This ratio can be explained by the optically thick molecular gas within GMCs. We show that the enhanced $R_{21/10}$ occurs at the downstream sides of the spiral arms. In the interarm regions farther away from the arms, $R_{21/10}$ becomes lower and is consistent with that observed in the MW and M51. The new example of $R_{21/10}$ variations emphasizes the importance of $R_{21/10}$ as a prime diagnostic tool of the physical condition of bulk molecular gas in galaxies.

2. Observations and Data Reduction

M83 was observed with the Total Power (TP) Array of ALMA in CO(1–0) and CO(2–1). After the data reduction described below, we analyze the data at the FWHM beam size of the CO(1–0) data, 56.″6 (∼1.2 kpc). Despite its lower spatial resolution, the analysis of single-dish data is an important first step for a solid confirmation of the variations of $R_{21/10}$, since interferometer data are susceptible to additional noise introduced in the imaging process. The data were reduced using the Common Astronomy Software Applications package (CASA; McMullin et al. 2007). The calibration was performed in the standard way as for the ALMA data reduction pipeline, with a more careful calibration of the relative flux scales among execution blocks (EBs; see below).

2.1. CO(1–0)

The CO(1–0) observations mapped a 11.′7 × 11.′7 area with the On-The-Fly (OTF) mapping technique along the R.A. and decl. directions. We obtained a total of 125 EBs, each of which, with a few exceptions, observed the whole area. We rejected five EBs due to bad weather (unreasonably low intensity), spurious pointing corrections (blurred map appearance), and relatively large flux errors with respect to the other EBs (deviations greater than a few %). The statistics of the 120 EBs are as follows: the average number of TP antennas was 3.71, the total observing and on-source times were 110.1 hr and 60.4 hr, respectively, and the system temperature $T_{\rm sys}$ was 99–129 K at the 10–90 percentiles. The ACA correlator was used to obtain spectra with band and channel widths of 250 MHz and 61 kHz.

Individual spectra were calibrated in the standard way. After the calibration they were re-sampled on a grid of pixel size 5.″62 using the prolate spheroidal function with a size of 6 pixels (Schwab 1980, 1984). The effective FWHM beam size after this regridding/smoothing is 56.″6. We generated separate datacubes for the 120 EBs, calculated the flux ratios and errors of all of their pairs, and solved for relative flux scales by inverting the design matrix. The derived scaling coefficients have a small scatter of only 1.3%. We applied these coefficients to co-add all the spectra into two datacubes for the R.A. and decl. scans. Spectral baselines were subtracted with straight lines. The two were combined with the Emerson & Graeve (1988) method. We converted the antenna temperature T_a^* into the main beam temperature $T_{\rm mb}$ using a main beam efficiency of 0.856 calculated from the Jy/K parameter from the observatory. The final cube has 3900 channels and an rms noise of ∼6.2 mK in $T_{\rm mb}$ in a velocity channel width of 0.159 km s^{-1}.

2.2. CO(2–1)

The CO(2–1) observations covered approximately a 8.′4 × 8.′4 region with a position angle of about 52°. The region was split into nine rectangular regions, each of which was observed separately. About 30% the area of each region overlaps with that of an adjacent region. The total number of EBs was 160. The average number of antennas per EB was 3.57. The total observing and on-source times were 132.8 hr and 66.4 hr. The $T_{\rm sys}$ was 59–89 K at the 10–90 percentiles. The band and channel widths were 2 GHz and 977 kHz or 1 GHz and 488 kHz.

All the data were reduced in the standard way. We generated 160 separate datacubes for all the EBs, calculated the flux ratios and errors of all their pairs when their spatial coverages overlapped, and solved for the relative flux scaling coefficients. The coefficients have a small scatter of 3.1%, and we made a correction for this before co-adding the data. We used a main beam efficiency of 0.836. The final datacube has 488 channels and an rms noise of ∼2.0 mK in $T_{\rm mb}$ with a pixel scale of 2.″81 and velocity channel width of 1.276 km s^{-1}.

2.3. The CO 2–1/1–0 Ratio ($R_{21/10}$)

The CO(1–0) and CO(2–1) datacubes were integrated along velocity without any clip/mask, to produce integrated intensity maps, $I_{\rm CO1-0}$ and $I_{\rm CO2-1}$ (Figures 1(a) and (b)). To match the spatial resolutions, the CO(2–1) map was smoothed by a sequence of a deconvolution with the CO(2–1) beam and convolution with the CO(1–0) beam. The beams here are generated by a convolution of the native telescope beam, approximated with a Gaussian (an FWHM of 58.″3 at 100 GHz), and the spheroidal function. The smoothed map was regridded to the pixel scale of the CO(1–0) map. The 1σ

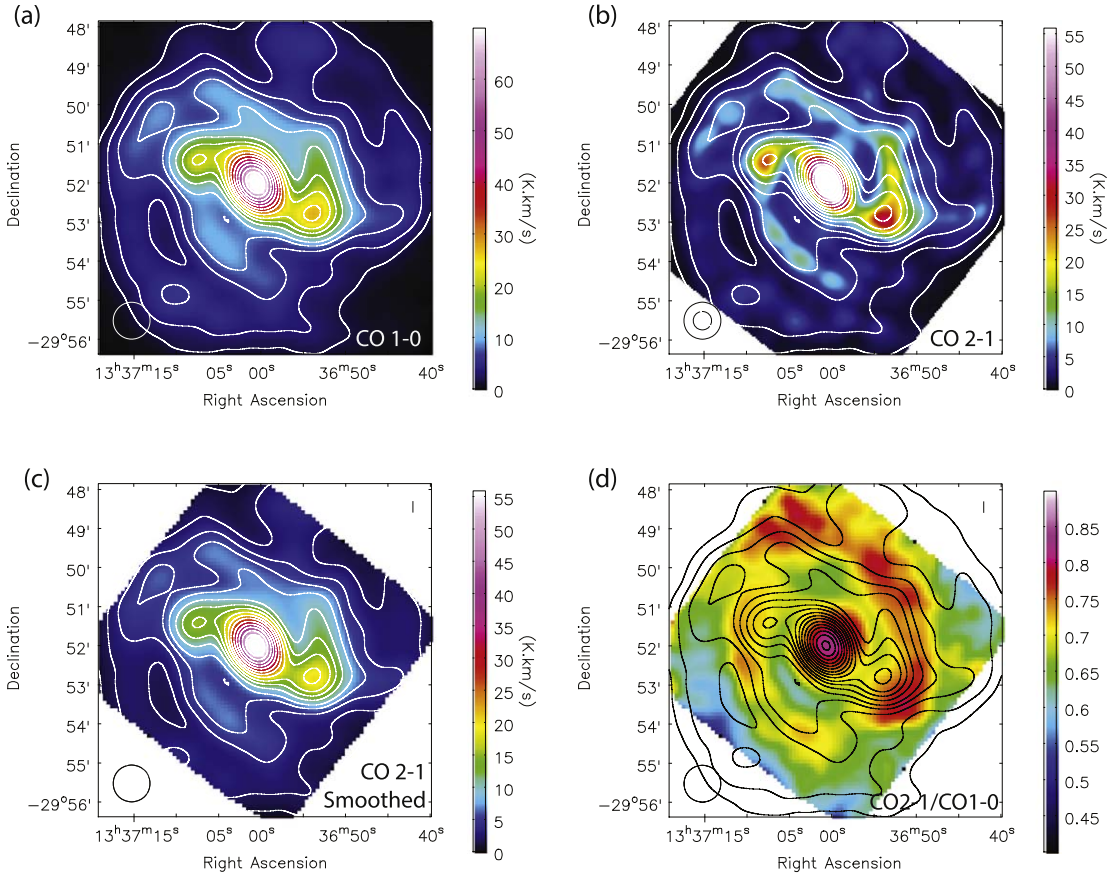

Figure 1. Maps of M83 in (a) CO(1–0), (b) CO(2–1), (c) CO(2–1) smoothed to the CO(1–0) resolution, and (d) CO 2–1/1–0 ratio ($R_{21/10}$). The contours are of CO(1–0) at 1.5, 3, 5, 7, 9, 12, 15, 18, 22, 26, 30, 35, 40, 45, 51, 57, and 63 K · km s^{-1}. The beam sizes of the original CO(1–0) and CO(2–1) maps (a and b) are indicated by circles (56.″6 and 28.″3, respectively). For panels (c) and (d), we trimmed the edges where the blank data outside the CO(2–1) field of view affect the smoothing.

noise is about 61 and 14 mK · km s^{-1} in I_{CO1-0} and I_{CO2-1}, respectively. The lowest CO(1–0) contour in Figure 1 is at about 25σ significance, and the same locations are at about 70σ significance in CO(2–1).

The CO(1–0) beam is larger than the CO(2–1) beam, and the edge of the smoothed map suffers from the absence of data beyond the field coverage. To quantify this effect, we applied the above smoothing procedure to an image with a uniform illumination over the field of view (i.e., the pixel value was set to 1 within the field of view and 0 outside). We used the pixels with a value greater than 0.99 after the smoothing. This reduced the field of view to about 7.′0 × 7.′0. The final CO(2–1) map is presented in Figure 1(c). The $R_{21/10}$ is calculated as I_{CO2-1}/I_{CO1-0} (Figure 1(d)). The random error in $R_{21/10}$ is about 4% at the lowest I_{CO1-0} contour or less at higher I_{CO1-0}.

These maps suffer from the systematic errors in absolute flux calibrations (about 5% according to the observatory), which, however, does not affect the relative variations of I_{CO2-1}, I_{CO1-0}, and $R_{21/10}$ within the maps. This 5% systematic uncertainty mainly comes from the uncertainty in the models of primary flux calibrators. It is likely to affect both I_{CO2-1} and I_{CO1-0} in a similar manner and, to an extent, cancel out in $R_{21/10}$. The sampling of these maps is redundant with a pixel scale of 5.″62 for a beam size of 56.″6. We use only every fifth pixel when they are correlated with other data (Section 3).

2.4. Ancillary Data

For comparisons, we obtained ancillary data from the archives: specific intensity (brightness) maps in *GALEX* far-ultraviolet (FUV; 1516 Å; I_{FUV}; Gil de Paz et al. 2007), in *Spitzer* 24 μm ($I_{24\mu m}$; Bendo et al. 2012b), and in *Herschel* 70 and 350 μm ($I_{70\mu m}$ and $I_{350\mu m}$; Bendo et al. 2012a). Their native resolutions are 4.2, 5.7, 5.6, and 24.″2, respectively. For comparisons with the CO data, they are smoothed to a Gaussian beam and convolved with Schwab's spheroidal function, resulting in a final beam size of 56.″6. The data are then regridded to the CO data grid.

3. Results

Figure 1 shows that the CO line ratio varies spatially between the galactic center and disk, and between the spiral arms and interarm regions. For comparison, the CO(2–1) map (Figure 1(b)) shows the locations of the molecular spiral arms. Both the average and median of $R_{21/10}$ in this region are 0.69. The observed range of ∼0.5–0.8 likely represents the upper and lower limits due to the low resolution (see discussions below). Still, it appears that $R_{21/10}$ varies from <0.7 in the interarm regions to >0.7 around the spiral arms—or more precisely, at the convex, presumably downstream,[26] sides of the spiral arms. This is consistent with the variations in the MW (Sakamoto et al. 1997) and in

[26] HII regions appear preferentially on the convex sides (Poetrodjojo et al. 2019), and hence we assume they are the downstream sides.

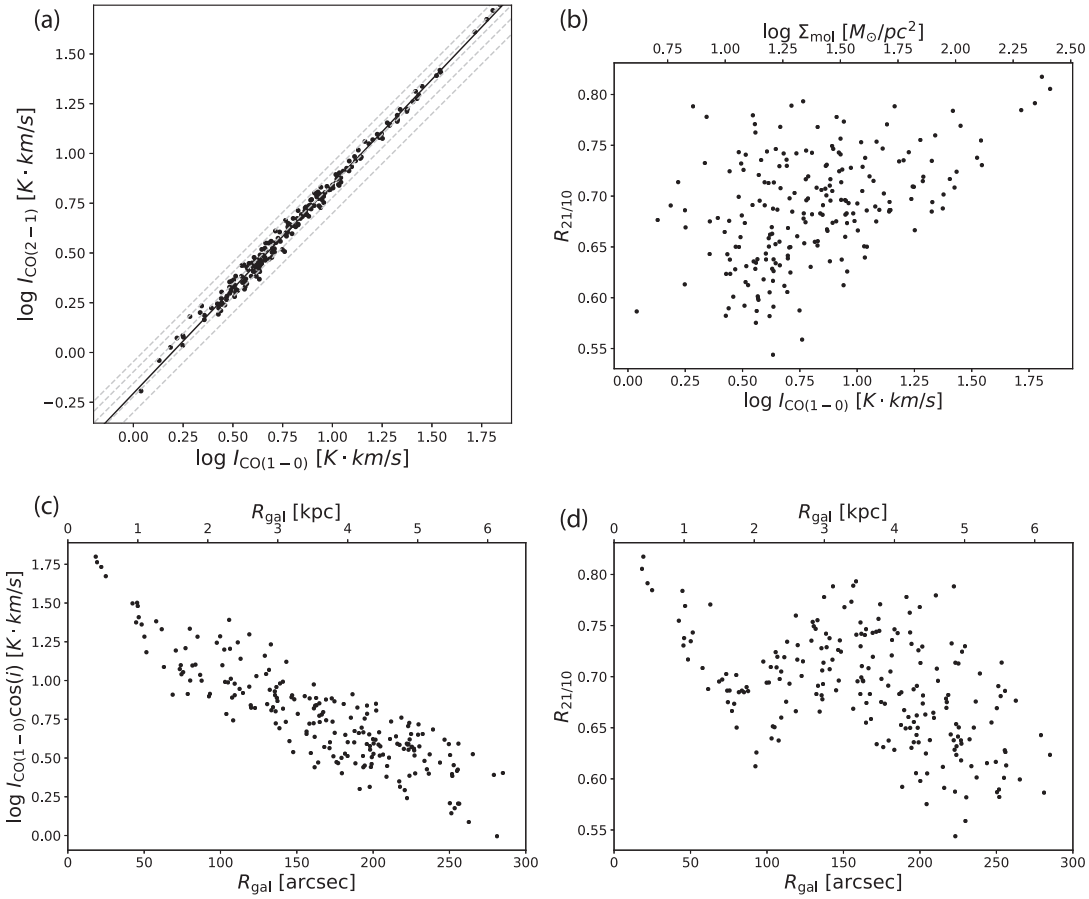

Figure 2. (a) I_{CO1-0} vs. I_{CO2-1}. Dashed lines represent $R_{21/10}$= 0.9, 0.8, 0.7, 0.6, and 0.5 (top to bottom). The solid line is a fit. (b) $R_{21/10}$ vs. I_{CO1-0} (Σ_{mol}). Radial profiles of (c) $I_{CO1-0}\cos i$ with inclination correction, and (d) $R_{21/10}$. The radius R_{gal} is calculated from the galactic center (RA, DEC) = (13:37:00.8, −29:51:58) using the inclination ($i = 25°$) and position angle (PA = 226°) from Crosthwaite et al. (2002). The random error in $R_{21/10}$ is < 4%. The maps in Figure 1 are spatially oversampled, and we use only every fifth pixel (about half-beam sampling) for these scatter plots.

M51 (Koda et al. 2012). The northwestern spiral arm shows a higher ratio than the southeastern arm. Along the arms, $R_{21/10}$ is approximately constant and does not show clear radial trends. $R_{21/10}$ is high >0.8 in the galactic center, as is also observed in the MW center (Oka et al. 1996; Sawada et al. 2001). It stays ∼0.7 along the bar.

Despite the low resolution, this analysis of single-dish data is an important first confirmation of the variations, since the flux calibration is fairly consistent over the galactic disk. It is still important to keep in mind that in Figure 1 the galactic structures, such as the spiral arms and interarm regions, are somewhat smeared due to the large beam size. The range of $R_{21/10}$, if it is observed at a higher resolution, would be wider, while the mean and median $R_{21/10}$ are less likely affected. The typical range of $R_{21/10}$ observed in the MW and in M51 at higher linear resolutions is 0.4–1.2, with only rare instances of >1. It is conceivable that the intrinsic range in M83 is similar to those in the MW and M51, but is smoothed to the observed range.

A non-LTE model suggests that $R_{21/10}$ depends primarily on the H_2 volume density n_{H_2} and kinetic temperature T_k for collisional excitation, and, on the CO column density N_{CO} per velocity (or optical depth) for photon trapping and radiative transfer, although this last factor is typically constrained within a relatively narrow range (Scoville & Solomon 1974; Goldreich & Kwan 1974; Solomon et al. 1987; Koda et al. 2012). Obviously, our spatial resolution element (or beam; ∼1.2 kpc) includes multiple GMCs (see Figure 1). Even the lowest contour corresponds to a molecular gas mass of $M_{mol} \sim 8 \times 10^6 M_\odot$ in one beam (using the conversion factor from Bolatto et al. 2013 to convert I_{CO1-0} into M_{mol} or molecular gas surface density Σ_{mol}). This M_{mol} is about 20 GMCs if all the emission is from GMCs analogous to a typical Galactic GMC ($4 \times 10^5 M_\odot$; Scoville & Sanders 1987). The n_{H_2} and T_k are the parameters *within* the GMCs. If we assume that all GMCs in each beam have the same average conditions, the factor of ∼2 change in $R_{21/10}$ roughly corresponds to changes of a factor of ∼2–3 in n_{H_2} and/or T_k in the GMCs (Koda et al. 2012).

I_{CO1-0} and I_{CO2-1} are tightly correlated (Figure 2(a)), while their ratio $R_{21/10}$ also changes with I_{CO1-0} (or Σ_{mol}; Figure 2(b)). The bottom-right part of this figure is empty as if the region below a diagonal line were avoided. The I_{CO1-0} is defined over a large beam, and hence, Σ_{mol} represents the average surface density in the environment of unresolved GMCs within the beam. In this plot, the $R_{21/10}$ is always high ($\gtrsim$0.7) in regions of high Σ_{mol} (or I_{CO1-0}). The GMCs within the beam have higher n_{H_2} and/or T_k on average when their environment is crowded with GMCs. On the other hand, the ratio is spread over a relatively wide range in regions of low Σ_{mol}. Even though the average environmental surface density is low, n_{H_2} and/or T_k within the underlying GMCs can vary from low to high, resulting in the spread in $R_{21/10}$.

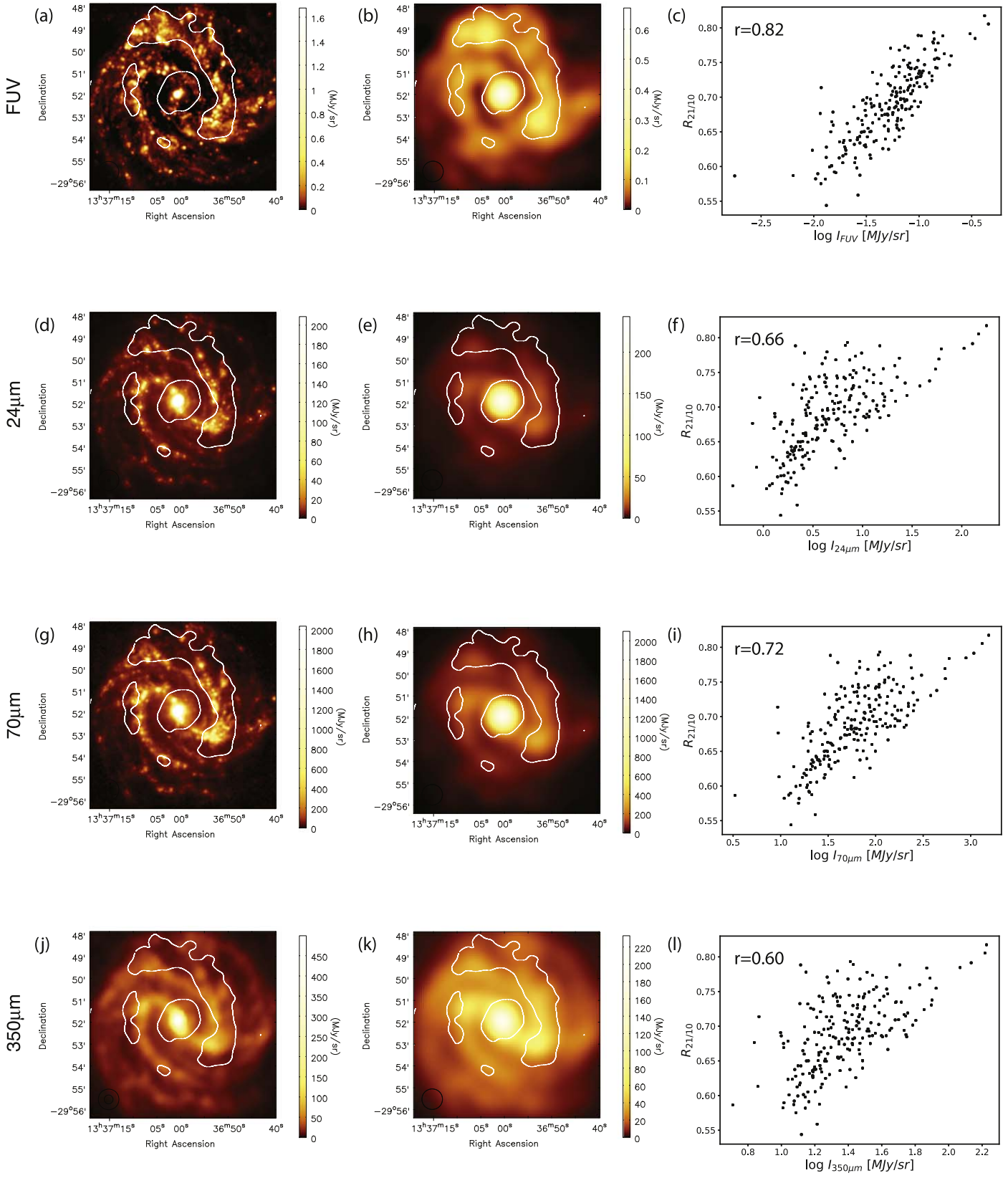

Figure 3. Rows 1-4: *GALEX* FUV, *Spitzer* 24 μm, *Herschel* 70 μm and 350 μm data. Column 1: images at the data's native resolutions of 4.2, 5.7, 5.6, and 24.″2 from top to bottom. Contours are at $R_{21/10} = 0.72$ to enclose the regions of high $R_{21/10}$. Column 2: images smoothed to the CO(1–0) resolution of 56.″6. Column 3: correlations between $R_{21/10}$ and each data in specific intensity. The correlation coefficients r are shown.

The radial profiles of I_{CO1-0} and $R_{21/10}$ are shown in Figure 2(c) and (d). An inclination correction is applied to I_{CO1-0}. I_{CO1-0} (and Σ_{mol}) decays exponentially with a scale length of $\sim$94″ ($\sim$2.0 kpc). Note that the profile of I_{CO2-1} is similar with a scale length of $\sim$88″ (1.9 kpc). $R_{21/10}$ peaks at the galactic center ($\gtrsim$0.8), decreases through the radius range

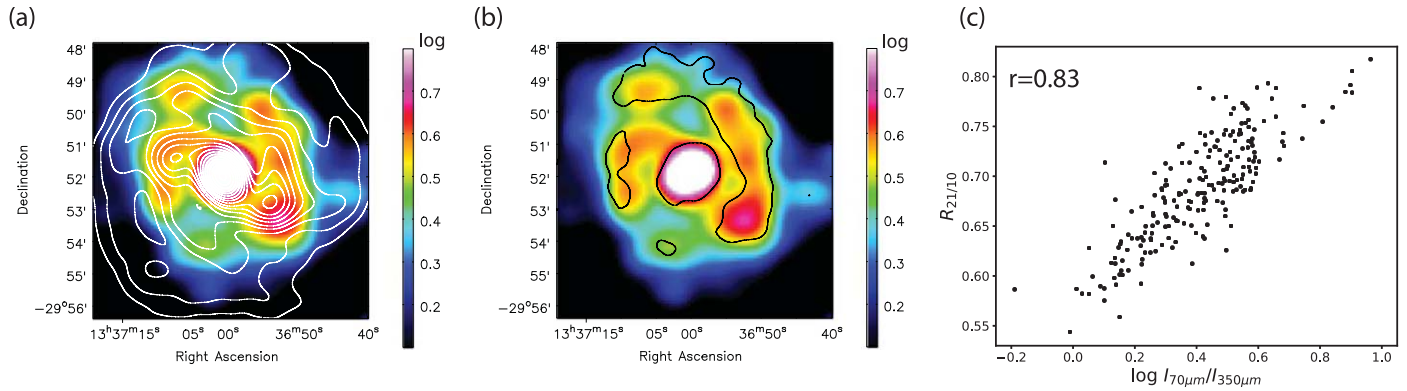

Figure 4. Comparisons with $\log(I_{70\mu m}/I_{350\mu m})$ (color), a proxy of dust temperature. The contours are (a) the CO(1–0) integrated intensity, and (b) $R_{21/10} = 0.72$. (c) $R_{21/10}$ vs. $\log(I_{70\mu m}/I_{350\mu m})$. Note that this dust color map is similar to a T_d map from spectral energy distribution fitting by Foyle et al. (2011).

Table 1
Results of Linear Regression

x	y	α	β	r
$\log I_{CO1-0}$	$\log I_{CO2-1}$	1.05	−0.205	1.00
$\log I_{CO1-0}$	$R_{21/10}$	0.219	0.511	0.45
$\log I_{CO2-1}$	$R_{21/10}$	0.190	0.565	0.53
$\log I_{FUV}$	$R_{21/10}$	0.161	0.897	0.82
$\log I_{24\mu m}$	$R_{21/10}$	0.137	0.596	0.66
$\log I_{70\mu m}$	$R_{21/10}$	0.134	0.448	0.72
$\log I_{350\mu m}$	$R_{21/10}$	0.242	0.355	0.60
$\log I_{70\mu m}/I_{350\mu m}$	$R_{21/10}$	0.292	0.569	0.83

Note. The gradient (α) and intercept (β) from the ordinary least squares bisector fitting (Isobe et al. 1990), and the correlation coefficient (r).

of the bar (∼0.65), increases again due to the spiral arms (∼0.75), and decreases toward the outskirts ($\lesssim$0.60). Note again that these are the ratios averaged over a 1.2 kpc beam.

Figure 3 compares $R_{21/10}$ with the FUV and infrared (IR) data. The contours in the left and middle columns indicate regions of high $R_{21/10}$. The FUV image shows a tighter spatial correlation with high $R_{21/10}$ than the IR images even though the FUV image suffers more from extinction. In particular, FUV and $R_{21/10}$ remain high at the downstream sides of the spiral arms. The right column shows correlations between $R_{21/10}$ and their specific intensities. The correlation coefficient r is shown in each plot (as well as in Table 1, which also lists the gradients and intercepts from linear regression). FUV presents the tightest correlation here as well. $R_{21/10}$ also correlates with the IR emissions. It is high in the regions of high $I_{24\mu m}$, $I_{70\mu m}$, and $I_{350\mu m}$, but shows relatively large spreads at low specific intensities [this is similar to what is seen with I_{CO1-0} (Σ_{mol})]. The regions of high $R_{21/10}$ at low IR intensities are a major contributor to the spreads in their correlations (i.e., top-left quartiles in Figure 3(f), (i), and (l)). Those regions tend to have low I_{CO1-0} and contribute also to the spreads in the correlation of $R_{21/10}$ and I_{CO1-0} (Figure 2(b)). On the other hand, they have high FUV intensities and lie on the tighter correlation of $R_{21/10}$ and FUV (Figure 3(c)). They tend to appear on the convex, downstream sides of the spiral arms, and might correspond to the "interarm" gas with an elevated $R_{21/10}$ found by Crosthwaite et al. (2002) and Lundgren et al. (2004).

FUV is expected to heat up dust grains, and in fact, $R_{21/10}$ also correlates well with $I_{70\mu m}/I_{350\mu m}$ (dust color, a proxy of dust temperature T_d; Figure 4). Here we choose 70μm and 350 μm to cover the expected range of T_d of around 10–40 K (using the peak of blackbody spectrum as a rough guideline). Theoretically, no efficient coupling mechanism between T_d and gas temperature T_k is identified yet (Goldreich & Kwan 1974; Scoville & Kwan 1976; Goldsmith & Langer 1978) at the average density of Galactic GMCs (∼300 cm^{-3}; Scoville & Sanders 1987). However, this correlation suggests a link, either directly or indirectly, between the dust heating by the interstellar radiation field (ISRF) and the condition of GMCs even after the passages of spiral arms.

4. Discussion

We showed a systematic trend that $R_{21/10}$ is elevated in regions of high Σ_{mol} (when they are averaged over a 1.2 kpc area), while its spread becomes large in environments of low Σ_{mol}. In particular, the high $R_{21/10}$ at low Σ_{mol} is not immediately expected and requires additional explanation. Such a condition is found mostly around the radial range of the spiral arms (Figure 2(d)). This high $R_{21/10}$ shows good quantitative and positional correlations with high I_{FUV} and T_d everywhere, including the downstream side of the spiral arms, better than with the IR intensities.

A possible explanation may be a potential direct thermal coupling between the dust, heated by ultraviolet photons, and the gas. Although no efficient mechanism has been identified (Goldsmith & Langer 1978), a potential mechanism might be a coupling through H_2O molecules—they may absorb dust radiation and heat up H_2 by collisional de-excitation (Scoville & Kwan 1976). Other possibilities are more indirect. GMCs may, in some way, remain dense and/or warm after spiral arm passage and maintain a high $R_{21/10}$ on a timescale of ∼100 Myr, which is about the lifetime of B stars, a source of bright FUV.

We could also speculate that the observed trend is related to the evolution of massive stars after arm passage. The massive stars are initially obscured in their parental clouds, contributing to the IR intensities through dust heating. They later escape the parental clouds and enhance the ISRF in-between GMCs (thus, high unobscured I_{FUV}) and probably the cosmic ray (CR) flux through subsequent supernovae explosions (which heat up the gas, leading to high $R_{21/10}$). These evolutionary phases, and hence the lags in time, would result in the spatial offsets of IR and FUV and keep $R_{21/10}$ enhanced toward the downstream sides of the spiral arms (see Egusa et al. 2004, 2009; Louie et al. 2013). The observed I_{FUV} varies by a factor of ∼30

(Figure 3(c)), and, presumably, the CRs follow a similar trend spatially and in flux. With numerical simulations, Peñaloza et al. (2017, 2018), and their series of papers, showed that $R_{21/10}$ is elevated in a stronger ISRF and/or at higher CR densities.

The analysis here is based on low-resolution ALMA single-dish data, but is an important first confirmation of the variations of $R_{21/10}$. Obviously, the analysis of one galaxy is limited and a larger sample is called for. ALMA, with its main interferometer, should be able to resolve $R_{21/10}$ variations on GMC scales (Hirota et al. 2018, showed this possibility). In this Letter, we did not consider the possibility that the *majority* of CO emission arises from the optically thin CO gas outside GMCs, which could also explain high $R_{21/10}$. Such a possibility can be tested when the GMCs are resolved.

This Letter makes use of the following ALMA data: ADS/JAO.ALMA#2013.1.01161.S, ADS/JAO.ALMA#2015.1.00121.S, ADS/JAO.ALMA#2016.1.00386.S, and ADS/JAO.ALMA#2017.1.00079.S. ALMA is a partnership of ESO (representing its member states), NSF (USA) and NINS (Japan), together with NRC (Canada), MOST and ASIAA (Taiwan), and KASI (Republic of Korea), in cooperation with the Republic of Chile. The Joint ALMA Observatory is operated by ESO, AUI/NRAO, and NAOJ. The National Radio Astronomy Observatory is a facility of the National Science Foundation operated under cooperative agreement by Associated Universities, Inc. J.K. acknowledges support from NSF through grant AST-1812847. The work of L.C.H. was supported by the National Science Foundation of China (11721303, 11991052) and the National Key R&D Program of China (2016YFA0400702). K.S. was supported by MOST 108-2112-M-001-015. We also thank the anonymous referee.

Facilities: ALMA, IRSA, *Spitzer*, *Herschel*.

Software: CASA 5.4.1-31 (McMullin et al. 2007).

ORCID iDs

Jin Koda https://orcid.org/0000-0002-8762-7863
Kazushi Sakamoto https://orcid.org/0000-0001-5187-2288
Samuel Boissier https://orcid.org/0000-0002-9091-2366
Daniela Calzetti https://orcid.org/0000-0002-5189-8004
Bruce G. Elmegreen https://orcid.org/0000-0002-1723-6330
Luis C. Ho https://orcid.org/0000-0001-6947-5846
Masato I. N. Kobayashi https://orcid.org/0000-0003-3990-1204
Sergio Martín https://orcid.org/0000-0001-9281-2919
Kazuyuki Muraoka https://orcid.org/0000-0002-3373-6538
Kouichiro Nakanishi https://orcid.org/0000-0002-6939-0372
Nick Scoville https://orcid.org/0000-0002-0438-3323
Mark Seibert https://orcid.org/0000-0002-1143-5515
Catherine Vlahakis https://orcid.org/0000-0003-3745-4228
Yoshimasa Watanabe https://orcid.org/0000-0002-9668-3592

References

Bendo, G. J., Boselli, A., Dariush, A., et al. 2012a, MNRAS, 419, 1833
Bendo, G. J., Galliano, F., & Madden, S. C. 2012b, MNRAS, 423, 197
Bigiel, F., Leroy, A., Walter, F., et al. 2008, AJ, 136, 2846
Bolatto, A. D., Wolfire, M., & Leroy, A. K. 2013, ARA&A, 51, 207
Crosthwaite, L. P., Turner, J. L., Buchholz, L., Ho, P. T. P., & Martin, R. N. 2002, AJ, 123, 1892
Dame, T. M., Ungerechts, H., Cohen, R. S., et al. 1987, ApJ, 322, 706
Egusa, F., Kohno, K., Sofue, Y., Nakanishi, H., & Komugi, S. 2009, ApJ, 697, 1870
Egusa, F., Sofue, Y., & Nakanishi, H. 2004, PASJ, 56, L45
Emerson, D. T., & Graeve, R. 1988, A&A, 190, 353
Falgarone, E., Panis, J. F., Heithausen, A., et al. 1998, A&A, 331, 669
Foyle, K., Rix, H.-W., Dobbs, C. L., Leroy, A. K., & Walter, F. 2011, ApJ, 735, 101
Fukui, Y., & Kawamura, A. 2010, ARA&A, 48, 547
Garcia-Burillo, S., Guelin, M., & Cernicharo, J. 1993, A&A, 274, 123
Gil de Paz, A., Boissier, S., Madore, B. F., et al. 2007, ApJS, 173, 185
Goldreich, P., & Kwan, J. 1974, ApJ, 189, 441
Goldsmith, P. F., & Langer, W. D. 1978, ApJ, 222, 881
Hasegawa, T. 1997, in IAU Symp. 170, CO: Twenty-Five Years of Millimetre-Wave Spectroscopy, ed. W. B. Latter et al. (Cambridge: Cambridge Univ. Press), 39
Heyer, M., & Dame, T. M. 2015, ARA&A, 53, 583
Hirota, A., Egusa, F., Baba, J., et al. 2018, PASJ, 70, 73
Isobe, T., Feigelson, E. D., Akritas, M. G., & Babu, G. J. 1990, ApJ, 364, 104
Koda, J., Scoville, N., Hasegawa, T., et al. 2012, ApJ, 761, 41
Leroy, A. K., Walter, F., Bigiel, F., et al. 2009, AJ, 137, 4670
Louie, M., Koda, J., & Egusa, F. 2013, ApJ, 763, 94
Lundgren, A. A., Wiklind, T., Olofsson, H., & Rydbeck, G. 2004, A&A, 413, 505
McMullin, J. P., Waters, B., Schiebel, D., Young, W., & Golap, K. 2007, in ASP Conf. Ser. 376, Astronomical Data Analysis Software and Systems XVI, ed. R. A. Shaw, F. Hill, & D. J. Bell (San Francisco, CA: ASP), 127
Nishimura, A., Tokuda, K., Kimura, K., et al. 2015, ApJS, 216, 18
Oka, T., Hasegawa, T., Handa, T., Hayashi, M., & Sakamoto, S. 1996, ApJ, 460, 334
Peñaloza, C. H., Clark, P. C., Glover, S. C. O., & Klessen, R. S. 2018, MNRAS, 475, 1508
Peñaloza, C. H., Clark, P. C., Glover, S. C. O., Shetty, R., & Klessen, R. S. 2017, MNRAS, 465, 2277
Poetrodjojo, H., D'Agostino, J. J., Groves, B., et al. 2019, MNRAS, 487, 79
Saintonge, A., Wilson, C. D., Xiao, T., et al. 2018, MNRAS, 481, 3497
Sakamoto, K. 2008, Ap&SS, 313, 245
Sakamoto, S., Hasegawa, T., Handa, T., Hayashi, M., & Oka, T. 1997, ApJ, 486, 276
Sakamoto, S., Hayashi, M., Hasegawa, T., Handa, T., & Oka, T. 1994, ApJ, 425, 641
Sandstrom, K. M., Leroy, A. K., Walter, F., et al. 2013, ApJ, 777, 5
Sawada, T., Hasegawa, T., Handa, T., et al. 2001, ApJS, 136, 189
Schwab, F. R. 1980, Optimal Gridding, Tech. Rep. 132, VLA, (Socoro, NM: National Radio Astronomical Observatory) https://library.nrao.edu/public/memos/vla/sci/VLAS_132.pdf
Schwab, F. R. 1984, in Indirect Imaging. Measurement and Processing for Indirect Imaging, ed. J. A. Roberts, 333
Scoville, N. Z., & Kwan, J. 1976, ApJ, 206, 718
Scoville, N. Z., & Sanders, D. B. 1987, in Interstellar Processes, ed. D. J. Hollenbach & H. A. Thronson, Jr. (Dordrecht: Reidel), 21
Scoville, N. Z., & Solomon, P. M. 1974, ApJL, 187, L67
Seta, M., Hasegawa, T., Dame, T. M., et al. 1998, ApJ, 505, 286
Solomon, P. M., Rivolo, A. R., Barrett, J., & Yahil, A. 1987, ApJ, 319, 730
Sun, J., Leroy, A. K., Schruba, A., et al. 2018, ApJ, 860, 172
Thim, F., Tammann, G. A., Saha, A., et al. 2003, ApJ, 590, 256
Vlahakis, C., van der Werf, P., Israel, F. P., & Tilanus, R. P. J. 2013, MNRAS, 433, 1837
Watson, L. C., & Koda, J. 2017, in Outskirts of Galaxies, Vol. 434, ed. J. H. Knapen, J. C. Lee, & A. Gil de Paz (Cham: Springer), 175
Yoda, T., Handa, T., Kohno, K., et al. 2010, PASJ, 62, 1277